Journal of Applied Physics ARTICLE scitation.org/journal/jap

The production of OH in a nanosecond pulsed helium plasma jet impinging on water, saline, or pigskin

Cite as: J. Appl. Phys. **131**, 173301 (2022); doi: 10.1063/5.0083568
Submitted: 27 December 2021 · Accepted: 17 April 2022 ·
Published Online: 2 May 2022

Meimei Lai,[1] Shutong Song,[1,2] Edwin Oshin,[1,2] Lucas Potter,[2] Nicola Lai,[3] and Chunqi Jiang[1,2,a)]

AFFILIATIONS

[1]Frank Reidy Research Center for Bioelectrics, Old Dominion University, Norfolk, Virginia 23529, USA
[2]Department of Electrical and Computer Engineering, Old Dominion University, Norfolk, Virginia 23529, USA
[3]Department of Mechanical, Chemical, and Materials Engineering, University of Cagliari, Cagliari 9128, Italy

[a)]**Author to whom correspondence should be addressed:** cjiang@odu.edu

ABSTRACT

Applications of plasma-induced biological effects via reactive oxygen and nitrogen species (RONS) make the non-thermal atmospheric-pressure plasma jets an appealing tool in biomedical fields. The presence of biological materials, especially as part of the electrode circuit, may change the plasma properties and impact on the production of RONS at the plasma–biomaterial interface. Effects of biomaterials on the production of hydroxyl radicals (OH) in a nanosecond pulsed, atmospheric-pressure plasma jet were investigated using a needle-to-plate electrode configuration with water, phosphate-buffered saline (PBS), or pigskin covering the ground plate. Driven by 200 ns, 7 kV pulses at 1 kHz, a helium plasma jet was generated between the hollow needle electrode and the biomaterial. Temporally resolved UV-visible imaging showed that the use of pigskin slowed down the streamer head propagation, whereas a more pronounced surface ionization wave was developed on the surface when water was used. The highest OH(A-X) emission above the biomaterial surface was observed using the PBS-covered electrode plate comparing to water or pigskin. Spatiotemporally resolved laser-induced fluorescence (LIF) showed that more OH was produced in the region near the needle electrode for both water and PBS, and the use of pigskin resulted in least OH production overall. In addition, measurements of H_2O_2 production in the liquid were used to determine the OH concentration in the vicinity of the biomaterial and agreed well with the relative OH-LIF measurements obtained at the gas–liquid interface for water and PBS.

I. INTRODUCTION

Nonequilibrium atmospheric pressure plasmas are known to produce reactive oxygen and nitrogen species (RONS) and induce biological effects via Redox chemistry[1] and, hence, have been proposed for a variety of biomedical applications including surface sterilization,[2,3] wound healing,[4–6] dental treatment,[7,8] and cancer therapy.[9,10] Among many RONS, OH was identified to be one of the most important short-lived radicals in water-containing plasmas and the primary building block of the formed H_2O_2,[11] who itself is considered an important agent in the chemical reactivity of plasmas in contact with water.[12,13] Production of OH by atmospheric pressure plasmas in contact with water has a strong dependence on plasma properties, e.g., electron temperature, density, and gas temperature.[14] Since plasma properties vary with modes of discharge, gas composition, and the electrode configuration, the use of different materials other than water will alter the electrode configuration or the circuit, influence the plasma properties, and, hence, impact on OH production. This modification of the electrode circuit during plasma formation due to different properties of target materials was discussed by Norberg *et al.*[15] and its influence on the electric field in the plasma and the plasma properties were also reported.[15–17] Riès *et al.* reported that the electrical conductivity (σ) of the plasma-impinging target influenced the production of OH by a μs-pulsed He plasma jet.[18] In their system, although the target (i.e., aqueous solutions, mouse skin, or the metal plate) was not designed to be part of the electrode circuit for plasma generation, the conductance of the target resulted in current flowing through the target to the ground and observed strong dependence of the plasma dynamics on target

conductivity.[18] Using another μs-pulsed He plasma jet with a similar electrode configuration, Yonemori *et al.* reported the effects of the surface condition of the target, i.e., a rat skin, glass, or melamine sponge, and the gas flow rate on the production of OH and O radicals and determined that the humidity of the surface and ambient air entrainment were additional factors that impact OH and O production for atmospheric pressure plasma jets.[19] Similar findings have also been reported by others.[18,20–22]

Laser-induced fluorescence (LIF) was frequently used for the quantification of OH densities in atmospheric pressure plasma jets.[18–21,23] OH-LIF allows time- and space-resolved measurements of ground-state OH density and has been applied for the evaluation of OH productions in APPJs.[24,25] However, this diagnostic method has several disadvantages. One is that determining the total density of OH(X) requires to collect fluorescence photons of all transitions, but typically there is only one transition being excited.[14] As a result, a model including all the transition states of the 3064 Å OH (A-X) system is typically employed in combination with the calibration of the detection system for absolute OH density measurements.[18,20] Another disadvantage of OH-LIF is the effect of collisional quenching, which can be upward quenching of the excited OH(A) transition to other excited or ionic states or downward quenching to the ground state OH(X) by collisions with other neutral molecules such as water.[14] For atmospheric pressure plasmas in contact with water, the quenching of the LIF signal due to humidity at the gas–liquid interface and in the plasma column makes the abolute calibration more difficult, and water density distribution needs to be determined independently.[18] Nevertheless, LIF is a relatively sensitive method to identify temporally and spatially resolved densities of ground state species and has less requirement on the spectral resolution of the detection system comparing to direct absorption techniques.[26]

Although the effect of target on OH production in atmospheric pressure plasma jets has been studied by many groups, these studies have mostly used μs-duration pulsed or radio frequency plasma jets. As the OH production depends on the driven pulse duration, especially when comparing 200 ns with 1 μs long pulses,[27] it is, hence, important to find out the effect of the target on OH distribution and production when the plasma jet is driven by shorter-duration pulses. In this study, spatiotemporally resolved emission profiles of OH (A-X) transition of the plasma jet impinging on water, phosphate-buffered saline (PBS) solution, or pigskin were compared to assess the effects of the biomaterial target on OH(A) production. The influence of the target on the axial-distribution and temporal development of the ground-state OH was evaluated using LIF, followed by a fluorometry method for liquid-phase H_2O_2 measurements. This indirect H_2O_2 kinetics-based method was to obtain the OH at the gas–target interface that was contributed to H_2O_2 formation in liquid[13,28] using fluorometry. For readers' convenience, a list of abbreviations/acronyms used here is listed in Table I.

TABLE I. List of the used abbreviations/acronyms in the alphabetical order.

Abbreviations/ Acronyms	Original words/Phrases
FWHM	Full width at half maximum
ICCD	Intensified charge-coupled device camera
LIF	Laser-induced fluorescence
ns-APPJ	Nanosecond pulsed atmospheric pressure plasma jet
OES	Optical emission spectroscopy
PBS	Phosphate-buffered saline
RONS	Reactive oxygen and nitrogen species
SIW	Surface ionization wave

II. EXPERIMENTAL DESIGN AND METHODS

A. Nanosecond pulsed plasma source and the biomaterial target

Atmospheric pressure microplasma jets driven by nanosecond high voltage pulses were previously produced using a single electrode.[29] By placing a grounded biomaterial target near the active nozzle electrode, the electrode system became a point-to-plate configuration except that the electrical properties (i.e., conductivity σ and relative permittivity ε_r) of the materials on the ground plate would affect the electrode circuit and discharge initiation. Similar nanosecond pulsed plasma sources have been reported previously.[27,30] A stainless steel hollow tube with an inner diameter of 0.25 mm and an outer diameter of 0.51 mm was used as the high-voltage electrode. A grounded plate holding the biomaterial target completed the circuit loop. The grounded copper plate was 1-mm thick and served as the bottom of a rectangular container, which was 75 mm in length, 25 mm in width, and 25 mm in height. The four sides of the container were made of 1 mm-thick fused-silica slides. For experiments using liquid, the container was filled with ultra-high purity water ($\varepsilon_r = 80$, $\sigma = 5.5\,\mu$S/m) or PBS solution (Fisher Scientific, $\varepsilon_r = 80$, $\sigma = 1.4$ S/m). The pigskin was previously harvested from a 1-yr-old miniature pig and stored in −20 °C. Prior to use, the skin was thawed in room temperature for 1.5 h until the tissue temperature reached an equilibrium at room temperature. For this study, the skin was dissected into smaller sample pieces to fit inside the container, with the outer layer or epidermis of the skin facing up toward the plasma and the inner or the dermis layer of the skin in contact with the copper bottom of the container. Three pigskin samples were prepared for each measurement. To reduce the variation in measurements, the skin samples were reduced to ∼6 mm thickness by removing the fatty tissue under the dermis layer. The ε_r and σ of the pigskin were estimated to be 10^3–10^4 and 0.2–0.3 mS/m, respectively.[31,32]

A high-voltage pulse generator (Direct Energy Incorporated, Model: PVX-4110), providing pulses having a full width at half maximum (FWHM) of 200 ns and a pulse amplitude of 7 kV at 1 kHz, was connected to the nozzle electrode via a 50-Ω coaxial cable. The voltage and current of the discharge were measured at the nozzle electrode using a high voltage probe (Tektronix 6015A) and a wideband current monitor (Pearson 6585) connected to a digital oscilloscope. Ultra-pure helium (99.999%, AirGas) was used as the working gas and flew through the powered hollow nozzle at a flow rate of 70 SCCM to produce a nanosecond pulsed atmospheric pressure plasma jet (ns-APPJ) impinging on a biomaterial target. The gap distance between the nozzle and the surface of the target was kept at 10 mm. The gas flow rate was controlled by a calibrated rotameter (Omega, 3841ST).

B. Imaging and spectroscopy measurements

Both high-speed imaging and spatiotemporally resolved optical emission spectroscopy (OES) were employed to evaluate the effect of the biomaterials on the development of the plasma. Details of the diagnostic systems were described previously.[27,30] The image of the plasma plume was taken with an exposure time of 5 ns by an intensified charge-coupled device camera (ICCD, Princeton Instrument PI-MAX 4) through a UV-visible, fused silica bi-convex lens (focal length = 75 mm). The ICCD was synchronized with the high-voltage pulse generator using a delay generator (Stanford Research Systems, DG 535). For emission spectroscopy, a 0.75 m Czerny–Turner monochromator (Princeton instruments, model SP2750) was coupled with the ICCD to collect the emission spectra from the ns-APPJ. A UV-enhanced two-mirror system (a plano and a concave mirror) with a 1:1 magnification was used to collect the plasma emission onto the entrance slit of the spectrometer, instead of the lens. The schematic of the OES experimental setup along with the electric measurements of the ns-APPJ is shown in Fig. 1(a). Similar optical systems for OES measurements were reported previously.[27,30] For this work, the slit width of the spectrometer was set at 20 μm. The ICCD exposure time was set at 8 s, which corresponds to a total of 8000 accumulations with the ns-APPJ operated at 1 kHz. The spatially integrated spectrum was obtained by integrating the spectrum over the axial distance between the HV nozzle and the target.

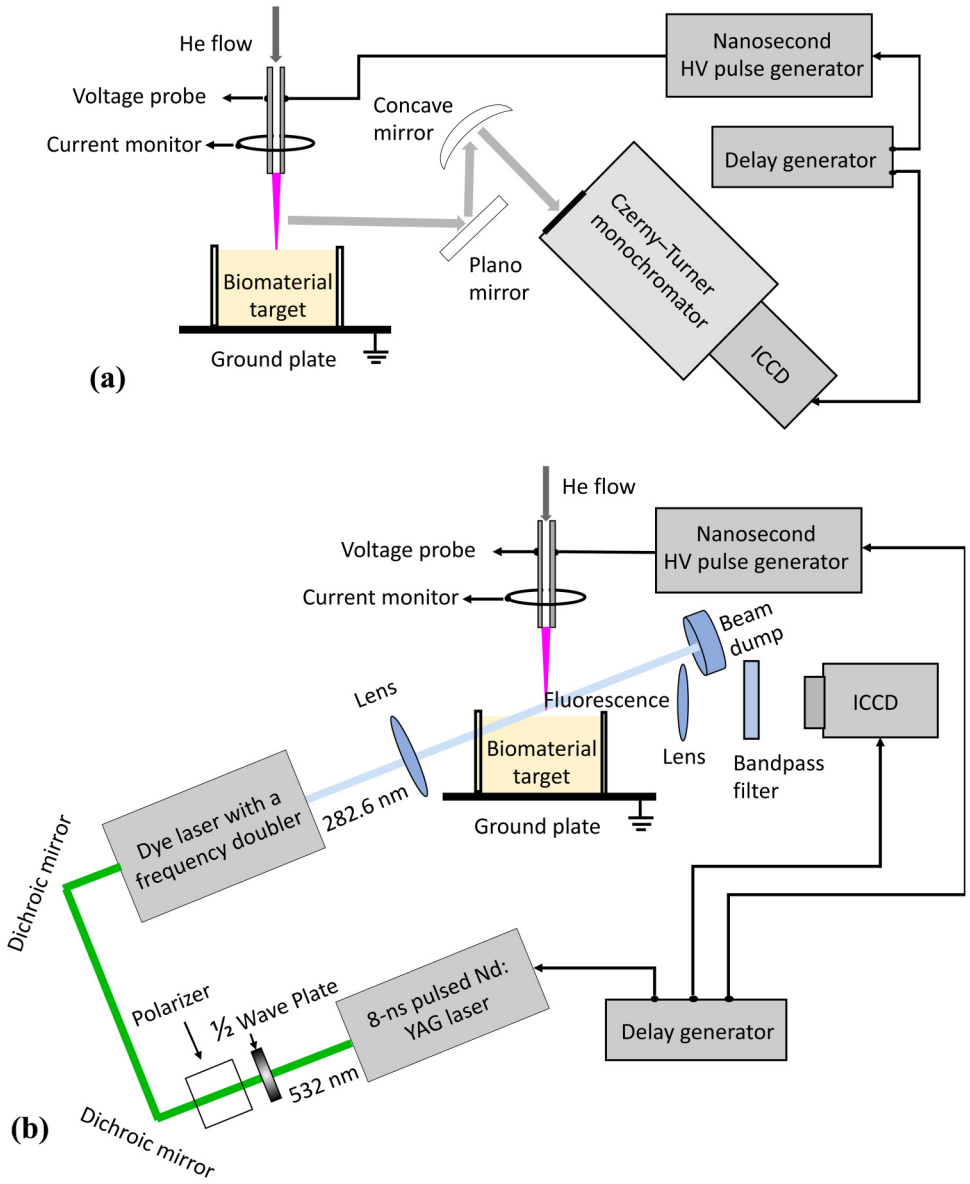

FIG. 1. Schematic of the experimental setup for (a) an OES measurement and (b) an LIF measurement of OH(X) in an ns-APPJ impinging on a biomaterial target.

The OH-LIF experimental setup is outlined in Fig. 1(b). The incident laser beam was generated by a dye laser (Spectra-Physics, Cobra-Stretch) that was pumped by a frequency-doubled Nd: YAG laser (Spectra-Physics, Pro-250) at 532 nm. The dye laser used Rhodamine 6G as the dye and was equipped with a frequency doubling crystal, allowing tuning of the laser wavelength between 280 and 288 nm and a linewidth of 2 pm. For LIF measurements, the center wavelength was set at 282.6 nm, corresponding to the excitation transition from OH $X^2\prod$ ($v'' = 0$) to OH $A^2\sum^+$ ($v' = 1$). The laser pulse had a FWHM of 8 ns and was operated at 10 Hz. The excitation laser beam was focused using a UV-visible lens (focal length = 50 cm; diameter = 25.4 mm) onto the plasma jet and the fluorescence was collected at a 90° angle using the ICCD after a bandpass filter centered at 309 nm with a FWHM of 10 nm. Similar as reported by others,[24] the strongest fluorescence was observed within 308 and 309 nm. The gate of the ICCD camera was set at 50 ns. The pulsed laser, ICCD, and the pulse generator powering the plasma were synchronized using the delay generator to obtain a temporally resolved LIF. The plasma was operated at 1 kHz, but the laser and ICCD were synchronized at 10 Hz. For every 100 pulses, the first pulse was performed with LIF and the rest were skipped. While the laser and ICCD only allow 10 Hz for optimal operation, the plasma jet can be operated at an either lower repetition frequency such as 10 Hz or higher one such as several kilohertz. We selected 1 kHz for the plasma operation frequency to have similar conditions to biomedical or environmental studies. The laser beam energy was fixed at 0.2 mJ and had a Gaussian beam width of 0.5 mm (based on $1/e$ of the maximum beam intensity with e being Euler's number), determined by Rayleigh scattering. The fluorescence was collected from a direction perpendicular to both the laser beam and the axial direction (z-direction) of the plasma jet. The center axis of the LIF collecting optics was aligned <1 mm above the target's surface.

C. High-resolution fluorometry for H_2O_2 measurement

The OH radicals generated by the ns-APPJ can interact with each other ($OH + OH \rightarrow H_2O_2$) or with water molecules ($OH + H_2O \rightarrow H_2O_2 + H$) to form H_2O_2.[13,28] It is, hence, possible to estimate the OH production at the gas–target interface by determining the H_2O_2 formation in liquid[9,13,28] using fluorometry. A fluorometer (O2k-Fluo LED2-Module) with a high-resolution respirometry apparatus (OROBOROS Instruments, Innsbruck, Austria) was used to measure the kinetics of H_2O_2, generated by the plasma, in ultra-pure water or PBS solution. Based on the protocol by Krumschnabel *et al.*,[33,34] the O2k-fluorometer detected the fluorescence from the highly colored resorufin compound, a widely used fluorophore, which was produced by the reaction between H_2O_2 and Amplex UltraRed (AmR, 10 μM) with horseradish peroxidase (HRP, 500 U per ml) as the catalyst. To collect the OH and H_2O_2 produced at the plasma–liquid interface, we placed the HV nozzle electrode 10 mm above the liquid surface, where the liquid, 10 ml in volume, was contained in the fluorometer chamber that served as a replacement for the rectangular container and the grounded target, as shown in Fig. 2(a). Although this setup allowed us to collect the radicals produced at the interface with minimum losses, the change in the circuit layout with the additional 4 mm-thick dielectric layer due to the use of a glass cuvette for the fluorometer system between the water/PBS and the grounding could impact the OH production and, hence, the measurement of H_2O_2. No difference was detected in the discharge voltage and current waveforms, nevertheless, comparing to that with the circuit layout without using the fluorometer. During the pulsed discharge, we expected that the voltage potential drop across this cuvette-induced capacitor was relatively small or negligible, especially comparing to the electrode gap and the sample itself. This was because that the cuvette-induced capacitance was relatively large comparing to that of the sample. The effect of the grounding difference on OH production and measurements was, hence, small or negligible. To collect OH and H_2O_2 generated on the skin surface, a plastic sampling tube was introduced around the electrode nozzle and the entrance of the fluorometer chamber, filled with ultrapure water of 10 ml, as shown in Fig. 2(b). This was to allow the gas phase radicals being mostly carried into the fluorometer by the He flow. A grounded and semi-rigid copper mesh, made of 25-gauge copper wire and with 56% opening, was used to hold the skin sample while allowing the passage of the gas flow. In addition, the temperature of the liquid was held at 37 °C with a constant

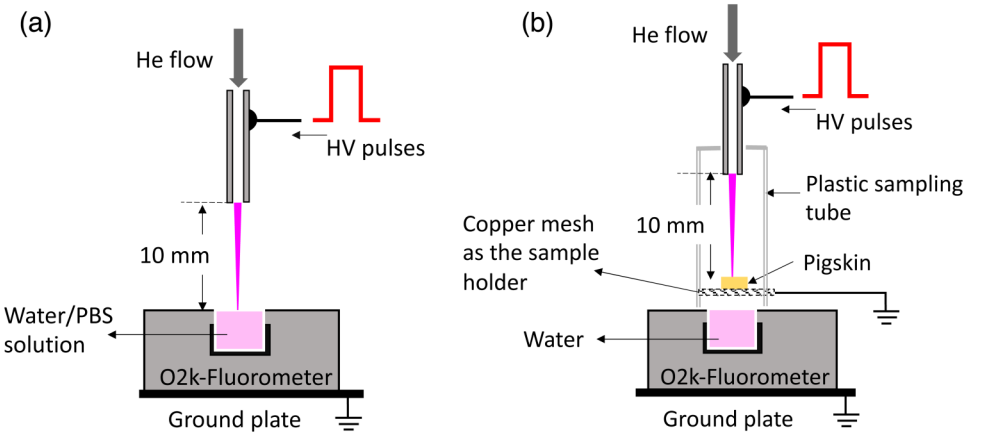

FIG. 2. Experimental setup of using an O2k-fluorometer to measure H_2O_2 generated by ns-APPJ impinging on (a) ultra-pure water or PBS solution and (b) pigskin.

stirring speed at 750 rpm for all measurements and calibrations. The fluorescence intensity was recorded until a steady state was reached to determine the H_2O_2 production rate in the liquid solution at each treatment condition. The intensity of the fluorescence emitted by resorufin was proportional to the concentration of H_2O_2 in the media,[34] and calibrations were conducted by adding 0.1 μM H_2O_2 to the solutions. The DatLab software (OROBOROS Instruments, Innsbruck, Austria) was used to calculate the real-time H_2O_2 molar flow rate from the time derivative of the resorufin signal.

III. RESULTS

A. Voltage and current waveforms

The typical discharge voltage and current waveforms of the ns-APPJ impinging on different targets were obtained, as shown in Fig. 3(a). For the same voltage pulse, the discharge current had small difference for using different biomaterial targets, which resulted in different energies per pulse: 32, 40, and 38 μJ for water, PBS, and pigskin, respectively. The energy per pulse was obtained by integrating the product of voltage and current over a sufficient period, e.g., 1.6 μs. The discharge current consisted of both displacement and conduction currents due to the capacitive circuit of the electrodes. Subtracting the current without the helium flow from the current with the helium flow, we obtained the jet current that corresponded to the conduction current, as shown in Fig. 3(b). By applying 7-kV, 200-ns FWHM pulses to the ns-APPJ system, the peak jet current was 59, 70, and 56 mA for water, PBS, and pigskin, respectively. It was evident that the highest energy per pulse and peak current were both obtained when PBS solution was used as the target.

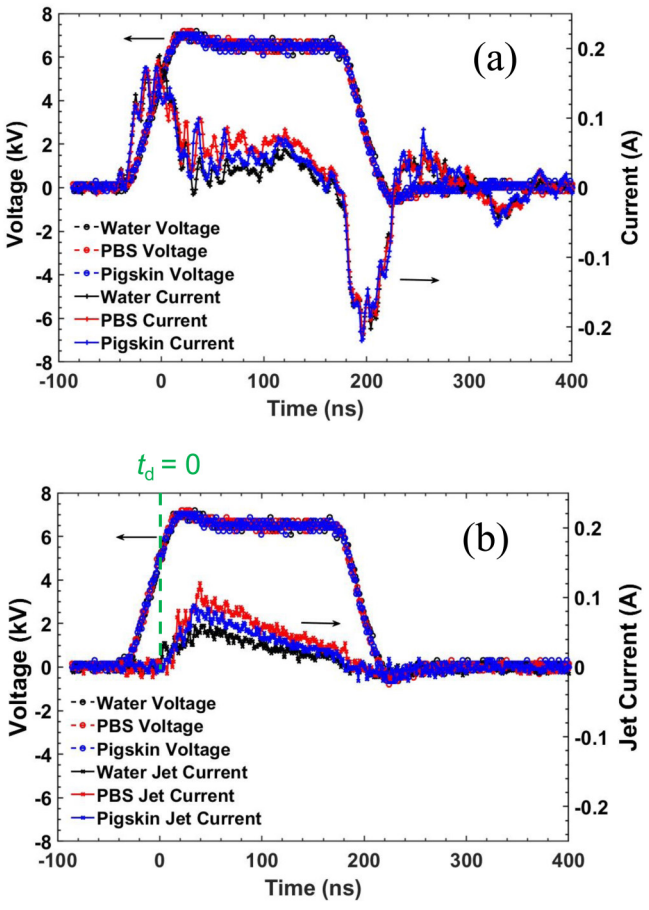

FIG. 3. Typical voltage and current waveforms of plasma impinging on water, PBS solution, and pigskin: (a) the discharge voltage and current; (b) the discharge voltage and jet current. The zero-delay time, $t_d = 0$, corresponds to the onset of the jet current.

B. Effects of the target on the ns-APPJ streamer and gas temperature

Temporally resolved plasma images of ns-APPJ impinging on water, PBS solution, or pigskin were taken at different delay times, as shown in Fig. 4. The delay time $t_d = 0$ was defined as the onset time of the jet current corresponding to a voltage of ~5 kV [Fig. 3(b)]. Comparing the streamer formation with jet current waveforms, the emission of plasma for any of the three targets was visible at the onset of current, reached its maximum intensity at the tip of the needle electrode when the current was at its peak value around $t_d = 45$ ns, and then started decaying from $t_d = 45$ to 175 ns until it was too low to be detected. The streamer coincided with the jet current and was only visible during the high pulsed voltage. At the beginning of streamer formation, the streamer head reached the surface of water or PBS solution at $t_d = 15$ ns, but it took extra 5 ns to reach the surface of pigskin. This indicates that the ionization wave propagates slightly slower for pigskin than water or PBS solution. After the streamer head reached the target surface, a conduction channel formed across the gap between the nozzle and the substrate, surface charging of the target would start and the current flow through the target would increase with the conductivity of the target. As shown in Fig. 4, the surface ionization wave (SIW), as discussed by Norberg *et al.*,[15] formed at the target surface, and it was more visible for water than PBS or pigskin, as the conductivities of the latter two were higher and the charge transferred to the surface was quickly depleted to the ground.

Time- and space-integrated optical emission spectra of ns-APPJ impinging on different targets were collected over the wavelength range of 200–850 nm to evaluate the effect of the target on the production of excited species. The total ICCD exposure time of 8 s and the full-length of the plasma jet between the needle and the target were used as time and space integration. Emissions from OH(A-X), N_2(C-B), N_2^+(B-X), He(^{3}D-^{3}P), and O(^{5}P-^{5}S) transitions were observed for the ns-APPJ impinging on all three targets, as shown in Fig. 5. The most prominent emission was from N_2(C-B) transition for all cases, and it was the highest for PBS solution, which was used as reference for normalization in Fig. 5. The excited OH(A) may relax to its ground state via OH(A-X) transition and can be observed via OES. A spatial profile of OH(A-X) emission along the z-axis was obtained, as shown in Fig. 6. The emission spectrum was time-integrated over the first 100 ns of the voltage pulse and space-integrated over a radial distance of ~1 mm.

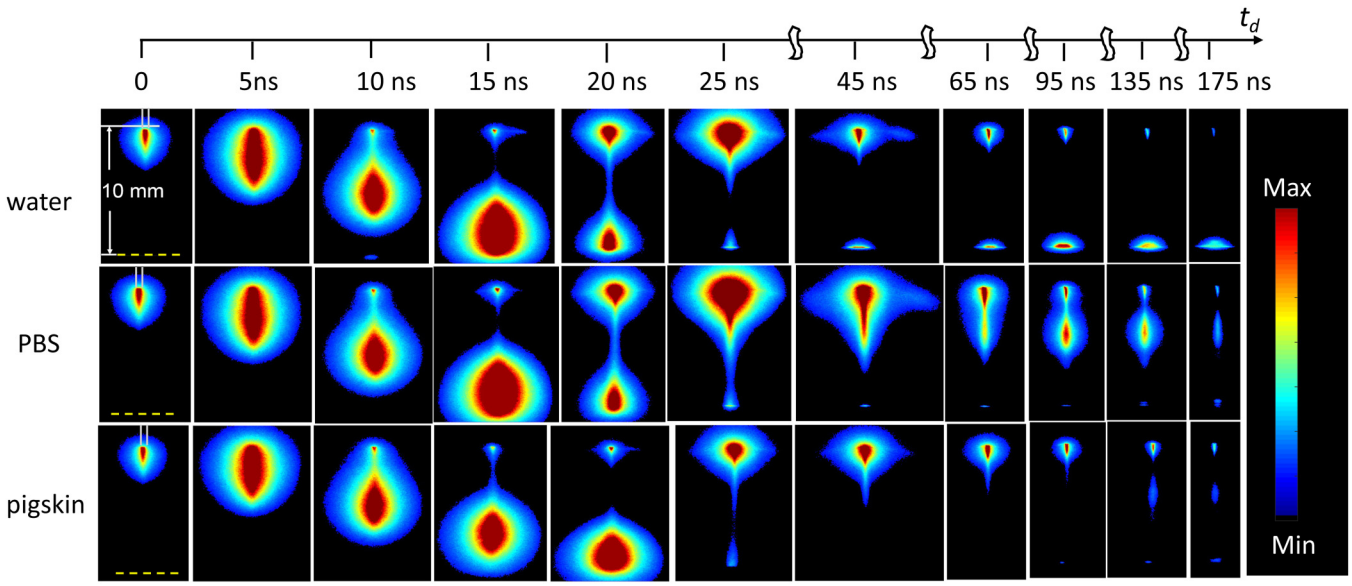

FIG. 4. Time-sequenced plasma images of ns-APPJ impinging on water, PBS solution, or the pigskin surface. The helium plasma jet was powered by 200-ns, 7-kV pulses at 1 kHz. The ICCD gate width was 5 ns with 100× gain. The gate was synchronized with the voltage pulse for various delay time, t_d, as labeled on the top of each image. The gap distance between the nozzle electrode and the target surface (both marked with light-colored lines in the images for $t_d = 0$) was 10 mm.

It showed that most OH(A-X) emission was near the high-voltage electrode nozzle for all targets, implying that the electron impact including dissociative excitation and dissociative electron–ion recombination[14] played important roles in OH(A) production. The electrons that enable these electron impact reactions must have the energy above the thresholds and are closely related to the external electric field strength. In addition, the quenching of OH(A) was expected to increase with the distance from the electrode nozzle due to collisions with N_2/O_2 and H_2O from air entrainment and biomaterial-induced humidity. Pigskin and water had comparable OH(A-X) emission, which was 67% of that for PBS. As PBS had the highest jet current and, hence, the highest ionization rate, the higher production of OH(A) could be obtained due to the increased electronic collisions near the electrode nozzle.

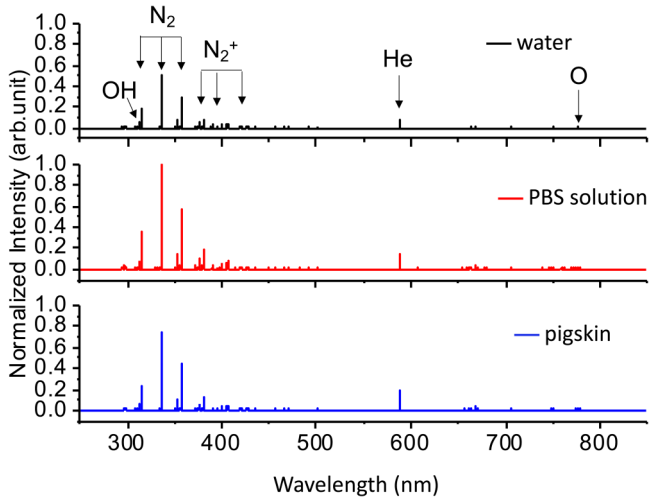

FIG. 5. Comparison of the integrated optical emission of ns-APPJ impinging on water, PBS solution, and pigskin.

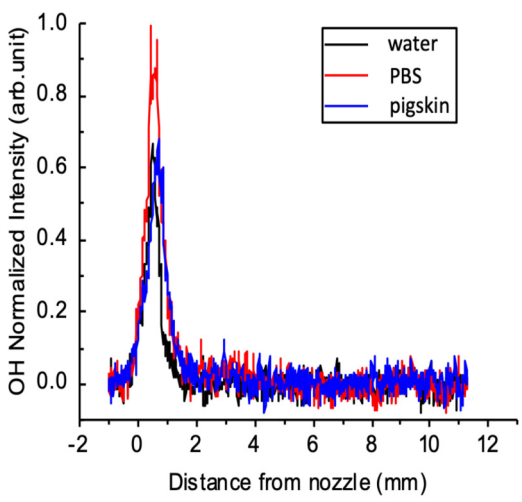

FIG. 6. Comparison of the OH(A–X) emission of ns-APPJ impinging on water, PBS solution, or pigskin as a function of the distance from the nozzle.

The gas temperatures of ns-APPJ impinging on different targets were measured by obtaining the rotational temperature of the second positive system of nitrogen. The emission from N_2(C–B) at (0–0) band transition was averaged over the entire length of the plasma jet and with a time integration of 8 s. The rotational temperature of 300 ± 25 K was obtained by comparing the measured and synthetic spectra, similar to what was reported previously.[29,30] No difference in the rotational temperature was observed for all targets used. In addition, as the gas temperature of the plasma could be assumed to be near the room temperature, it was feasible to use a GaAs-based fiber optic temperature probe (Neoptix T1S-2 M) to measure the temperature by transversally placing the tip of the probe in the plasma jet and 1 mm above the target surface. The average temperature out of three repeated measurements was 34.3, 34.7, and 40.4 °C for water, PBS, and pigskin with a maximum measurement error of 9%. The temperature was the highest for pigskin and almost the same for water and PBS. We also measured the surface temperature of the target during the plasma treatment and found the average temperature dropped to 21.0, 21.0, and 23.0 °C at the surface of water, PBS, and pigskin, respectively. The change of the surface temperature of the target was small, less than 3 °C, even after 50 min exposure to the plasma, which was operated at the same condition as imaging experiments. The small increase in temperature was expected as the average power (≤40 mW) of the ns-APPJ was relatively low. The heat produced onto the sample surface was quickly dissipated through convection (for the case of water or PBS) and conduction onto the grounding copper plate.

C. Effects of the target on ground-state OH production

The time-evolution and spatial distribution of the OH-LIF for ns-APPJ impinging on water were studied. The ICCD exposure time was set at 50 ns and the OH-LIF in each measurement was, hence, integrated over a 50 ns-duration. The time-window of 50 ns was chosen empirically based on the sensitivity of the system; it was the minimal time needed to obtain a sufficiently strong LIF signal while still allowing temporal studies. At a constant delay time, the fluorescence profile was identified radially symmetric. A symmetric radial profile of the OH-LIF in ns-APPJ impinging on water was reported previously,[35] which agreed with the results reported by others.[20,21] We, hence, focus here on the OH-LIF measurements at the radial center, $r = 0$. Figure 7(a) shows the temporal development of the OH-LIF at the radial center ($r = 0$) and the axial locations $z = 1.5$ and 8.5 mm, where $z = 0$ and 10 mm correspond to the surfaces of the nozzle and the target, respectively. It was evident that at both locations the OH-LIF peaked between 40 and 90 ns during which the jet current was also the highest. Although the OH-LIF decays with jet current decreasing, the fluorescence signal at both locations was visible after the jet current and voltage vanished ($t_d = 200$ ns). At the location near the nozzle, the OH-LIF was visible until 375 ns. The results suggested that the lifetime of the ground state OH was >175 ns. Comparing the temporal development of the OH-LIF at two locations, higher OH-LIF was observed at $z = 1.5$ mm. This agreed with the spatial distribution of the OH-LIF along the z-axis, as shown in Fig. 7(b), where two peaks in the axial profile of the LIF intensity were observed at $t_d = 40$ ns. The maximum LIF intensity, also the first peak, in the intensity distribution was observed at $z = 1.5$ mm, located at the region near the nozzle. The second peak in the LIF intensity, located at $z = 8.5$ mm and near the water surface, was 62% of the maximum intensity.

To evaluate the effect of the target on OH production, the time evolution and spatial distribution of OH-LIF for ns-APPJ impinging on water were compared with PBS solution and pigskin. Attentions were particularly paid at the region near the

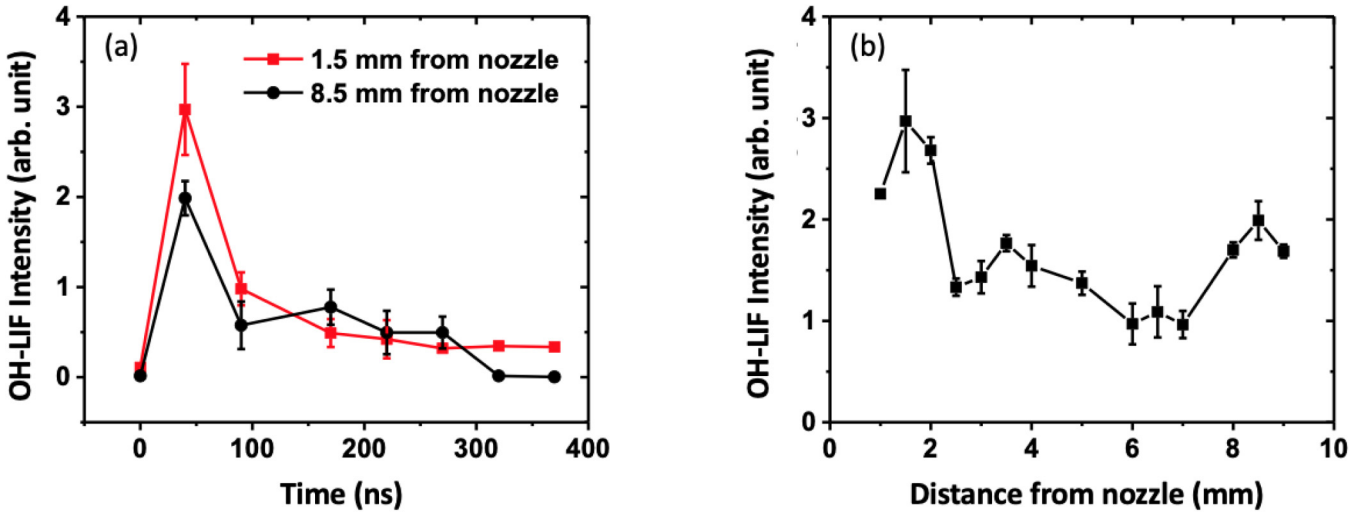

FIG. 7. Time-evolution and the axial profile of the OH-LIF emission from ns-APPJ impinging on water: (a) the time-evolution of the LIF at $r = 0$ and $z = 1.5$ and 8.5 mm; (b) the axial distribution of the LIF at $t_d = 40$ ns and $r = 0$.

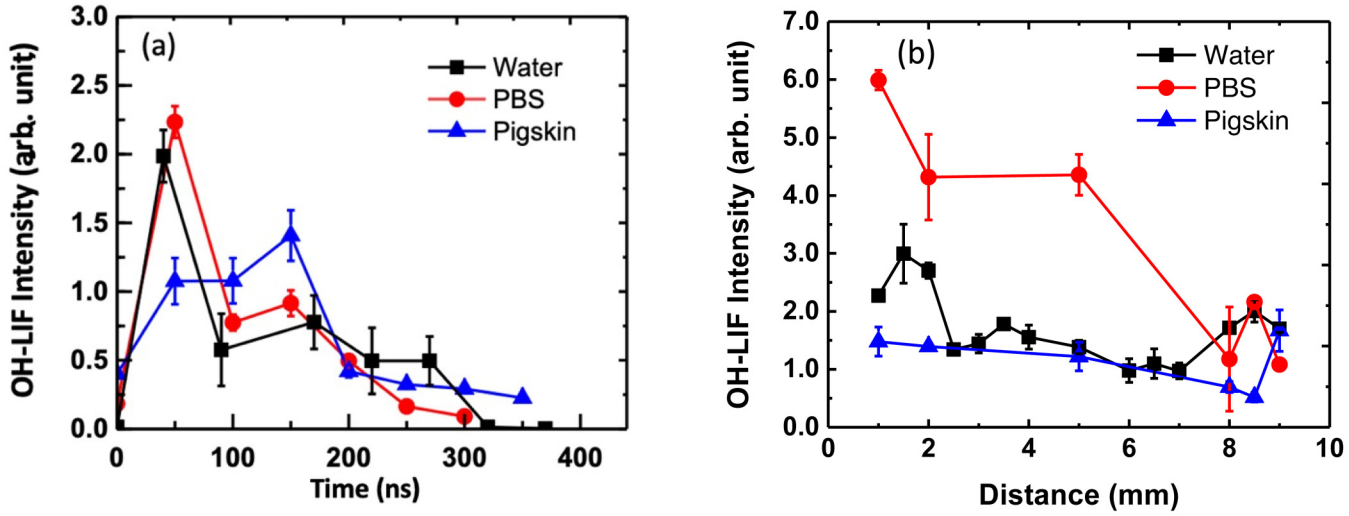

FIG. 8. Comparison of the time-evolution and the axial profile of OH-LIF emissions with ns-APPJ impinging on different biomaterial targets: (a) the time-evolution of the LIF at $r = 0$ and $z = 8.5$ mm; (b) the axial distribution of the LIF at $t_d = 40$ ns for water, 50 ns for PBS solution, and pigskin.

gas–target interface and the time when the maximal OH-LIF was observed. Figure 8(a) shows the temporal development of OH-LIF at the radial center and $z = 8.5$ mm (or 1.5 mm above the target surface) when ns-APPJ was impinging on different targets. The maximum fluorescence was reached at $t_d = 50$ and 150 ns for PBS solution and pigskin, respectively. Comparing with the peak intensity time for ns-APPJ impinging on water, PBS solution was slightly behind water for about 10 ns, and skin was more than 100 ns later. In addition, the OH-LIF for pigskin had the lowest peak value comparing to that for water or PBS solution. The intensity peak value was comparable for water and PBS solution although it was slightly higher for PBS. The spatial profile of OH-LIF along the center axis was obtained for ns-APPJ impinging on water, PBS solution, or pigskin at $t_d = 40$ or 50 ns, as shown in Fig. 8(b). Near the electrode nozzle, i.e., between z = 1 and 2 mm, PBS solution had the highest LIF intensity, 2 times or 4 times that of the maximal OH-LIF intensity for water or pigskin, respectively. The OH-LIF intensity for PBS solution decreased sharply with z. Near the target surface, at $z = 8$–9 mm, the OH-LIF intensity was comparable for all three targets, which was 1/4 or 1/3 of the intensity near the nozzle electrode for PBS solution or water and comparable or slightly higher for pigskin.

D. Effects of the target on the production of H_2O_2 in liquid

The absolute H_2O_2 production rate in 10-ml solution for ns-APPJ impinging on water, PBS, or pigskin was measured using fluorometry. For each condition, the measurement was repeated three times. The fluorometry signal, recorded with a helium flow without plasma, was used as the background. When the plasma was turned on, a significant increase in the H_2O_2 production rate was observed for all three cases. The ns-APPJ treatment operated at 1 kHz resulted in a H_2O_2 production rate of 0.20 ± 0.03, 0.21 ± 0.04, and 0.024 ± 0.003 nmol min^{-1} ml^{-1} for water, PBS solution, or pigskin, respectively. The H_2O_2 production rates were calculated by subtracting the value corresponding to the background signal from that observed when plasma was present. Assuming the production rate of H_2O_2 in the plasma-activated liquid was linearly dependent on pulse repetition frequency,[35] 33, 35, or 4 fmol of H_2O_2 would be generated by each pulse for ns-APPJ impinging on water, PBS, or pigskin, respectively. It was evident that H_2O_2 production was comparable for water and PBS but was nearly one-tenth less for pigskin.

IV. DISCUSSION

In this study, the biomaterial target covered the ground plate and served as part of the electrode circuit for ns-APPJ generation. The conductivity of the biomaterial had strong influence on the energy deposition of the plasma. As the σ of PBS was three or five orders of magnitude of skin or ultra-pure water, the use of PBS solution as the target resulted in 5% or 25% more in energy per pulse than skin or water, respectively. The relative permittivity of the target, on the other hand, had effects on discharge formation. It was observed that the streamer head propagated slower for pigskin than water or PBS. This was due to the difference in the establishment of the reduced electric field in the air gap between the electrode nozzle and the target. The ε_r of skin is >10 times higher than water or PBS. It, hence, took longer time to establish the electric field in the air gap for pigskin than water or PBS since the electromagnetic wave propagated slower in a medium with a higher ε_r. In other words, the actual voltage potential across the air gap rose slower for higher ε_r with the same input voltage pulse. It was found that higher dV/dt or shorter rise time of the voltage pulse

favored faster streamer propagation due to a higher reduced electric field established during breakdown.[29] It was also true, however, that higher capacitance would result in less voltage drop across the target and, hence, more potential difference across the air gap. As the capacitance of the air gap was much smaller than that of either water/PBS or pigskin, the differences in the voltage drop across the air gap before the streamer initiation for the three targets were, hence, negligible. Instead, the slowing-down effect in dV/dt due to the higher permittivity of pigskin was playing a more important role and resulted in the slower propagation of the streamer head for plasma impinging on pigskin comparing to water or PBS.

Over the gap between the electrode and target, PBS had the highest OH production, followed by water. At the location near the nozzle, the OH-LIF for PBS was twice of that for water and four times of that for pigskin. The peak OH-LIF intensity for pigskin was lower than water or BPS, which agreed with the findings by others.[19] Approaching the target surface, the OH-LIF intensity for both PBS and water decreased sharply with the distance to the target surface decreasing and became comparable to that of skin near the surface. Wu *et al.* reported that the OH production increased with water moisture of the target at a low gas flow rate,[20] which agreed with our flow condition. However, as the quenching coefficient for OH with H_2O was more than 5 times higher than that with N_2/O_2 molecules,[36] the high H_2O content at the gas–liquid interface would increase the quenching for OH, resulting in reduced sensitivity of the OH-LIF measurements[19,37] comparing to the gas–skin interface. This implied that the OH production at the plasma–liquid interface would have been higher than what we observed for water and PBS. The humidity near the target surface and differences in the OH quenching played critical roles for OH quantification using LIF. Nevertheless, it was evident that the use of pigskin as the target was associated with the least ground state OH production comparing to PBS or water even after considering the quenching effect.

The average absolute OH density produced by ns-APPJ impinging on different targets could be estimated from the measurements of H_2O_2 kinetics in liquid. Following Zhao *et al.* that 70% H_2O_2 was formed by the recombination of OH at the gas–liquid interface[28] and assuming all H_2O_2 at the interface dissolved into liquid due to the very high Henry's constant of H_2O_2 in water,[9,38] 1.4 mol OH would be needed to generate 1 mol H_2O_2 in the liquid. To calculate the gas density, the gas volume involved in the H_2O_2 production was estimated. As the OH-LIF measurements indicated, OH was produced along the air gap between the nozzle and the target, and higher densities were near the nozzle for water or PBS. In addition, a small amount of H_2O_2 could form from OH recombination near the nozzle, be carried to the target surface by the He flow, and contribute to the total H_2O_2 production measured in water, since the lifetime of H_2O_2 was found much longer than several seconds.[39] We, hence, used the entire air gap ($z = 10$ mm) for the volume to calculate the average OH density. Using a radius of 0.5 mm for OH-LIF,[23] a gas volume of 7.9 mm^3 was obtained. As a result, the average density of OH was estimated to be 3.6×10^{12}, 3.8×10^{12}, and 0.4×10^{12} cm^{-3} for water, PBS, and pigskin, respectively. The estimated average OH densities are about one-tenth of what was reported by Riès *et al.*[18] or Wu *et al.*[20] This discrepancy was likely due to the overestimation of the gas volume that was used to calculate the H_2O_2 production in liquid from OH. For the gas flow rate of 70 SCCM, the average flow velocity from the nozzle was 23 m/s. However, the gas flow velocity decreases substantially after the gas exits from the nozzle. A fluid modeling using COMSOL® software showed that the average flow around the radial center, within the cross section of the nozzle aperture, was less than 5 m/s. This means that it would take at least 2 ms for a neutral particle to cross the 10-mm air gap and reach the target surface from the nozzle. As the duration of OH production was less than 400 ns [Fig. 8(a)], it was, hence, not possible for OH formed near the nozzle to reach the target surface, and the majority of H_2O_2 formed in the gas–liquid interface was due to the direct recombination of OH produced locally. In addition, the H_2O_2 kinetics-based OH measurements showed that the average OH density for pigskin was one-tenth of water or PBS, whereas the OH-LIF indicated that the OH density for pigskin was the least of the three but was on the same order of magnitude as others. This difference was possibly due to the different collecting techniques used in the fluorometry for pigskin vs water/PBS. The use of the helium flow as the carrier gas and the sampling tube to collect the radicals from the skin surface, placed above the fluorometer liquid, might have resulted in significant loss of short-lived OH radicals during the sampling process. In fact, almost no OH radicals could directly be transferred into the fluorometer due to their short lifetime and fast recombination process on the surfaces of the sampling tube, and mainly long-lived H_2O_2 that was formed from OH at the skin surface could be carried over and reach the fluorometer entrance. Liquid-trapping-based sampling technique may improve the sampling efficiency and will be reported in the near future.

Both OH-LIF and fluorometry-based H_2O_2 measurements showed that the conductivity of the target played only a small role in OH production possibly by increasing the ionization rate and energy deposition in the plasma, as evidenced in the cases using PBS solution vs ultra-pure water. On the other hand, the humidity at the gas–target interface and the water content in the target played a more significant role in OH production comparing to conductivity; more OH would be produced when ns-APPJ was used to treat cells in a buffer solution, as in a typical *in vitro* setting, than to treat less humid materials such as skin or tissue, as for *ex vivo* or *in vivo* tests.

V. CONCLUSION

The effects of the biomaterial target on the streamer development, OH production in the gas phase, and H_2O_2 production in liquid were evaluated for the ns-APPJ impinging on water, PBS solution or pigskin. Although a similar behavior in streamer propagation was observed, the streamer head propagated slightly slower when the plasma was impinging on pigskin. More pronounced surface ionization wave was developed on the water surface when the plasma was impinging on ultra-pure water. The conductivity of the target had a significant impact on the energy deposition and ionization rate of the plasma. The strongest OH(A-X) emission was recorded near the proximity of the high-voltage nozzle electrode and during the rising phase of the voltage pulse. OH-LIF was detected over the entire space between the nozzle electrode and the target, and higher OH(X) productions were found near the nozzle

electrode for both PBS and water. The use of pigskin as the target resulted in the least OH(X) production and PBS being the highest. In addition, the measurement of the H_2O_2 production rate in fluorometer liquid also showed that ns-APPJ impinging on PBS produced the most OH radicals at the gas–liquid interface, closely followed by water, and the least for pigskin. Due to the use of a different sampling technique for pigskin from water or PBS, the loss of short-lived OH radicals during the sampling procedure might have resulted in substantially less H_2O_2 production being measured for pigskin using fluorometry. Importantly, this study demonstrated that OH production in the gas phase could be estimated with H_2O_2 measurements in liquid although more calibrations were needed to consider the transfer efficiency when the OH was not produced directly on the solvent of the fluorometer chamber. An average OH density could be determined using the H_2O_2 measurements with an LIF calibration obtained at a constant humidity condition, which will be considered in our future studies.

ACKNOWLEDGMENTS

The work was supported by the United States Air Force Office of Scientific Research under AFOSR Award No. FA9550-17-1-0257. The authors would like to thank Dr. Siqi Guo and Ms. Megan Scott for their help with the access to the pigskin.

AUTHOR DECLARATIONS

Conflict of Interest

The authors have no conflicts to disclose.

DATA AVAILABILITY

The data that support the findings of this study are available from the corresponding author upon reasonable request.

REFERENCES

[1]D. B. Graves, Phys. Plasmas **21**(8), 080901 (2014).
[2]M. Laroussi, Plasma Processes Polym. **2**(5), 391 (2005).
[3]J. U. Neuber, S. Song, M. A. Malik *et al.*, IEEE Trans. Radiat. Plasma Med. Sci. **1**(4), 368 (2017).
[4]B. Haertel, T. v. Woedtke, K.-D. Weltmann *et al.*, Biomol. Ther. **22**(6), 477 (2014).
[5]S. Bekeschus, A. Schmidt, K.-D. Weltmann *et al.*, Clin. Plasma Med. **4**(1), 19 (2016).
[6]N. Eswaramoorthy and D. R. McKenzie, Biophys. Rev. **9**(6), 895 (2017).
[7]C. Jiang, M.-T. Chen, A. Gorur *et al.*, Plasma Processes Polym. **6**(8), 479 (2009).
[8]C. Schaudinn, D. Jaramillo, M. O. Freire *et al.*, Int. Endod. J. **46**(10), 930 (2013).
[9]M. Keidar, R. Walk, A. Shashurin *et al.*, Br. J. Cancer **105**(9), 1295 (2011).
[10]D. Yan, J. H. Sherman, and M. Keidar, Oncotarget **8**(9), 15977 (2017).
[11]D. X. Liu, P. Bruggeman, F. Iza *et al.*, Plasma Sources Sci. Technol. **19**(2), 025018 (2010).
[12]B. R. Locke and K. Y. Shih, Plasma Sources Sci. Technol. **20**(3), 034006 (2011).
[13]P. Lukes, E. Dolezalova, I. Sisrova *et al.*, Plasma Sources Sci. Technol. **23**(1), 015019 (2014).
[14]P. Bruggeman and D. C. Schram, Plasma Sources Sci. Technol. **19**(4), 045025 (2010).
[15]S. A. Norberg, E. Johnsen, and M. J. Kushner, J. Appl. Phys. **118**(1), 013301 (2015).
[16]N. Y. Babaeva and M. J. Kushner, J. Phys. D: Appl. Phys. **43**(18), 185206 (2010).
[17]M. Hofmans and A. Sobota, J. Appl. Phys. **125**(4), 043303 (2019).
[18]D. Riès, G. Dilecce, E. Robert *et al.*, J. Phys. D: Appl. Phys. **47**(27), 275401 (2014).
[19]S. Yonemori and R. Ono, J. Phys. D: Appl. Phys. **47**(12), 125401 (2014).
[20]F. Wu, J. Li, F. Liu *et al.*, J. Appl. Phys. **123**(12), 123301 (2018).
[21]I. Yagi, R. Ono, T. Oda *et al.*, Plasma Sources Sci. Technol. **24**, 015002 (2015).
[22]Y. Yue, X. Pei, D. Gidon *et al.*, Plasma Sources Sci. Technol. **27**, 064001 (2018).
[23]L. Li, A. Nikiforov, Q. Xiong *et al.*, Phys. Plasmas **20**(9), 093502 (2013).
[24]T. Verreycken, R. Mensink, R. v. d. Horst *et al.*, Plasma Sources Sci. Technol. **22**(5), 055014 (2013).
[25]S. Kanazawa, H. Kawano, S. Watanabe *et al.*, Plasma Sources Sci. Technol. **20**(3), 034010 (2011).
[26]P. Bruggeman, G. Cunge, and N. Sadeghi, Plasma Sources Sci. Technol. **21**, 035019 (2012).
[27]S. Song, E. B. Sözer, and C. Jiang, Jpn. J. Appl. Phys. **58**(6), 066002 (2019).
[28]Y. Y. Zhao, T. Wang, M. P. Wilson *et al.*, IEEE Trans. Plasma Sci. **44**(10), 2084 (2016).
[29]C. Jiang, J. Lane, S. T. Song *et al.*, J. Appl. Phys. **119**(8), 083301 (2016).
[30]C. Jiang and S. Song, Jpn. J. Appl. Phys. **56**(4), 046101 (2017).
[31]C. Gabriel, A. Peyman, and E. H. Grant, Phys. Med. Biol. **54**(16), 4863 (2009).
[32]P. J. Bruggeman, M. J. Kushner, B. R. Locke *et al.*, Plasma Sources Sci. Technol. **25**(5), 053002 (2016).
[33]G. Krumschnabel, M. Fontana-Ayoub, Z. Sumbalova *et al.*, Methods Mol. Biol. **1264**, 245 (2015).
[34]M. Makrecka-Kuka, G. Krumschnabel, and E. Gnaiger, Biomolecules **5**(3), 1319 (2015).
[35]C. Jiang, E. B. Sözer, S. Song *et al.*, Phys. Plasmas **27**(11), 113513 (2020).
[36]M. Tamura, P. A. Berg, J. E. Harrington *et al.*, Combust. Flame **114**(3), 502 (1998).
[37]Q. Xiong, A. Y. Nikiforov, L. Li *et al.*, Eur. Phys. J. D **66**(11), 281 (2012).
[38]R. Sander, Atmos. Chem. Phys. **15**(8), 4399 (2015).
[39]J. Winter, H. Tresp, M. U. Hammer *et al.*, J. Phys. D: Appl. Phys. **47**(28), 285401 (2014).